JACS
JOURNAL OF THE AMERICAN CHEMICAL SOCIETY
pubs.acs.org/JACS

Open Access
This article is licensed under CC-BY 4.0

Article

Ammonia-Assisted Chemical Vapor Deposition Growth of Two-Dimensional Conjugated Coordination Polymer Thin Films

Jinxin Liu,[‡] Shuai Fu,[‡] Yubin Fu,[‡] Yunxu Chen, Kian Tadayon, Mike Hambsch, Darius Pohl, Ye Yang, Alina Müller, Fengxiang Zhao, Stefan C. B. Mannsfeld, Lei Gao, Mischa Bonn, Xinliang Feng,* and Renhao Dong*

Cite This: *J. Am. Chem. Soc.* 2025, 147, 18190−18196

Read Online

ACCESS | Metrics & More | Article Recommendations | Supporting Information

ABSTRACT: As emerging electroactive materials, the controlled synthesis of highly ordered two-dimensional (2D) conjugated coordination polymer (c-CP) films ensuring the long-range π-electron delocalization is essential for advancing high-performance (opto-)electronics. Here, we demonstrate the growth of highly crystalline 2D c-CP thin films on inert substrates by chemical vapor deposition with the assistance of ammonia (NH_3) for the first time, leveraging its deprotonation effect on ligands and competing effect as additional coordinating species. The resulting Fe-HHB (HHB = hexahydroxybenzene) films exhibit large-area uniformity and a 2 order-of-magnitude increase in crystal grain size, which translates into significant improvements in electrical conductivity (from 0.002 to 3 S/cm), charge mobility, elastic modulus, and hardness. To verify the generality of this NH_3-assisted synthesis, the contrast Cu-HHB and Cu-BHT (BHT = hexathiolbenzene) 2D c-CP thin films are also prepared and deliver significantly improved electrical conductivities from 51 to 113 and from 595 to 905 S/cm, respectively. The greatly improved crystallinity, combined with the high compatibility of the developed synthetic strategy with current device integration technologies, paves the way for developing c-CP-based electronics.

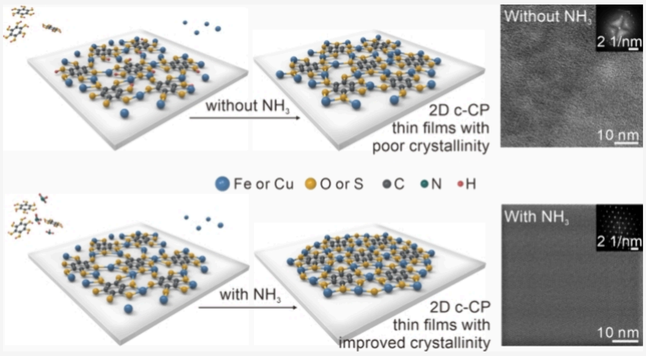

INTRODUCTION

Electrically conductive coordination polymers (ECCPs) and metal−organic frameworks (MOFs) are emerging electroactive materials that have garnered increasing attention in (opto-)electronics and spintronics.[1−3] Benefiting from the in-plane π-extended conjugation and out-of-plane $\pi-\pi$ interactions, two-dimensional (2D) conjugated CPs (c-CPs) exhibit many intriguing properties,[4,5] including excellent electrical conductivities (up to 10^3 S cm^{-1}),[6] remarkable charge mobility (up to 10^2 cm^2 V^{-1} s^{-1}),[7] superconductivity,[8] high photosensitivity,[9] and intrinsic ferromagnetic ordering.[10] These characteristics make them potential active layers for a wide range of electronic applications. As a prerequisite for their practical applications, achieving the rational synthesis of high-crystallinity 2D c-CP thin films that allow for the long-range π-electron delocalization and scalable device integration is crucial but remains a major challenge for conventional solution-based approaches.[11]

Reassembly of delaminated 2D c-CP nanosheets enabled straightforward mass production of their thin films but suffered from poorly controlled crystallinity and thicknesses.[11] To date, most 2D c-CP thin films utilized in fundamental studies and electronic applications have been synthesized at the liquid−liquid or gas−liquid interfaces, which enabled the large-scale production of film samples with variable thicknesses.[5,12] However, homogeneous nucleation of crystals in solutions generally led to particle contamination,[13,14] which could compromise the charge transport properties due to the extrinsic charge scattering, thereby restricting device performance. In addition, solution-induced corrosion and surface-tension effects further hindered the integration of the synthetic materials into nanodevices.[15] Chemical vapor deposition (CVD) could offer a solvent-free approach to ensure the formation of uniform thin films with a residual-free surface and atomic-level conformality.[16] Featured by large-area deposition and high controllability of crystal growth,[17,18] the incorporation of CVD and 2D c-CP thin films facilitates seamless compatibility with existing microfabrication technologies,[19,20] positioning it as an ideal methodology to advance the transition of 2D c-CPs into industrial electronics. Pioneering success was achieved in the growth of crystallized Cu-BHT

Received: March 19, 2025
Revised: May 7, 2025
Accepted: May 8, 2025
Published: May 15, 2025

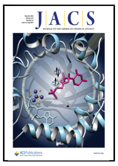

© 2025 The Authors. Published by American Chemical Society

https://doi.org/10.1021/jacs.5c04515

(BHT = hexathiolbenzene) thin films with a defect-engineered semiconductor−conductor transition[21] and crystallized Cu-THQ (THQ = tetrahydroxy-1,4-benzoquinone) thin films with a unique edge-on orientation.[22,23] Thereafter, the growth of patterned Cu-BHT films[19] and 2D c-CP thin films with ultrasmooth surfaces[20] further enhanced the compatibility with device integration. Despite the significant advances in the CVD synthesis of c-CP films, the realization of high crystallinity with large-sized crystalline domains has remained a great challenge, which also exerts a substantial impact on device performance.

Herein, we report the controlled CVD growth of high-quality 2D c-CP films on inert substrates using ammonia (NH_3) gas to aid in the deprotonation of ligands. The residual protons would act as electrostatic hindrances and obstruct the assembly of organized coordination networks,[24] ultimately resulting in low-crystallinity 2D c-CP films (Figure 1a). Conversely, deprotonation facilitated by the presence of NH_3 would favor the orderly assembly of precursors, leading to thin films with significantly improved crystallinity (Figure 1b). In addition, NH_3 can also act as an additional coordinating species to compete with metal−ligand interactions, promoting the reversible formation and breakage of the coordination bonds, thereby leading to high-quality 2D c-CPs. Considering the high dissociation energy of the Fe−O bond (Table S1), Fe-HHB (HHB = hexahydroxybenzene) is selected as the most ideal prototype material to maximize the competing effect of NH_3. Compared to the one synthesized in the absence of NH_3 (named **Fe-HHB-o**), the resulting thin films grown in the presence of NH_3 (named as **Fe-HHB-w**) exhibit an ~2 order-of-magnitude increase in the grain area (increased from ~10^2 to ~10^4 nm^2), leading to substantial improvements in conductivity (from 0.002 to 3 S/cm), mobility (from ~12 to ~31 $cm^2/(V \cdot s)$), elastic modulus (from ~25.7 to ~43.8 GPa), and hardness (from ~0.9 to ~2.0 GPa). Moreover, the electrical conductivities of the CVD Cu-HHB and Cu-BHT thin films were increased from ~51 and ~595 to ~113 and ~905 S/cm, respectively, after adopting the NH_3-assisted strategy. The contrast results confirm that the NH_3-assisted synthesis can be applicable to the preparation of various 2D c-CP thin films with improved quality, validating the universality of the proposed strategy.

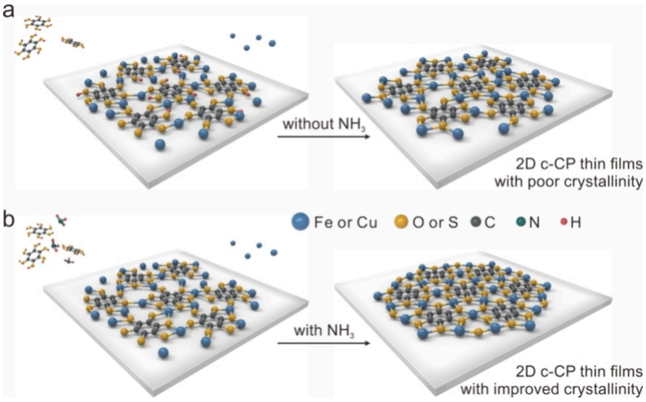

Figure 1. Schematic illustration of (a) the CVD growth process on an inert substrate without NH_3, resulting in 2D c-CP thin films with poor crystallinity and (b) the NH_3-assisted growth process, resulting in thin films with highly improved crystallinity. Here, the structure of Fe-HHB is used as the prototype to illustrate the growth strategy.

■ RESULTS AND DISCUSSION

The CVD growth of **Fe-HHB-w** was performed on SiO_2/Si or quartz substrates based on an optimal face-to-face inner tube system[21,22] (Figure 2a and Figure S1), while the sample synthesized without this face-to-face system shows inferior quality (Figure S2). Tris(acetylacetonato) iron(III) (Fe(acac)$_3$) and HHB powders were employed as precursors (Figure 2b), and a container of 0.14 mol/L $NH_3 \cdot H_2O$ was placed upstream, with a small opening to allow the steady release of NH_3 gas into the chamber under low pressure (~0.5 mbar). The as-grown **Fe-HHB-w** thin films exhibit visually uniform reflectivity across the ~1 cm^2 substrate areas, as evidenced by the macroscopic images (Figure 2c). The optical microscopy (OM) and scanning electron microscopy (SEM) images (Figure 2d and Figure S3) at low magnification indicate uniform contrast across the entire covered region, further affirming the uniform feature of the films. The uniform elemental distribution was also demonstrated by SEM-based energy-dispersive X-ray spectroscopy (EDX) elemental mapping (Figure 2e). In addition, no obvious signal assigned to the N element was detected in the EDX spectra (Figure S4), suggesting that no unintended doping occurred from NH_3. As revealed by atomic force microscopy (AFM), a continuous uniform Fe-HHB thin film with a thickness of ~11.5 nm was formed after a reaction time of 10 min (Figure 2f), which further increased to ~633.2 nm after a 6 h growth with the surface roughness R_q value reaching ~8 nm (Figures S5 and S6). Raman spectroscopy was utilized to characterize the coordination information on the synthesized **Fe-HHB-w** film.

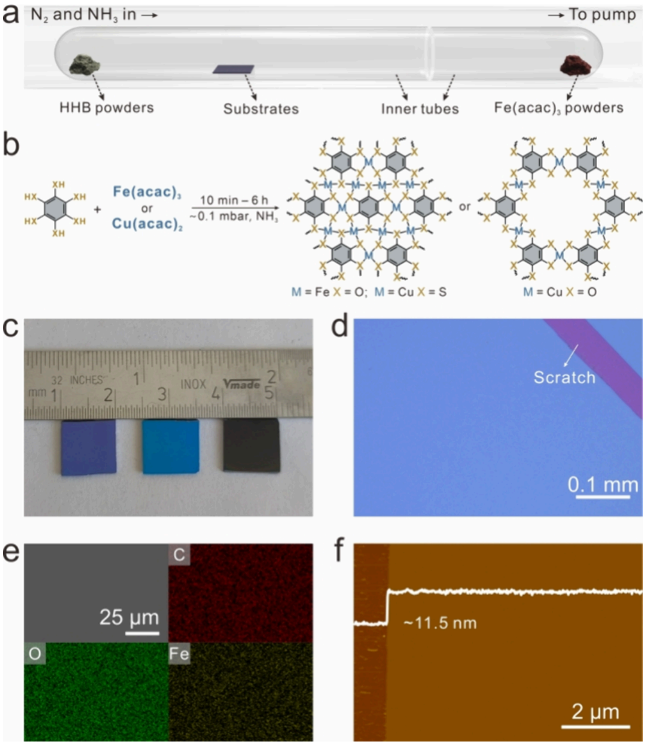

Figure 2. (a) Illustration of the typical CVD setup to perform the NH_3-assisted growth process. (b) Reaction scheme illustrating the NH_3-assisted synthesis of 2D c-CPs via coordination between HHB or BHT and Fe(acac)$_3$ or Cu(acac)$_2$. (c) Digital photography image, (d) OM image, (e) SEM image and corresponding EDX elemental mapping, and (f) AFM image of the as-grown **Fe-HHB-w** thin films.

The disappearance of the signal assigned to the O−H bond at ∼3300 cm^{-1} suggests the efficient coordination between Fe and substitution groups in the presence of NH_3 (Figure S7).[25] The homogeneous Raman intensity mapping also verifies the structural uniformity of the film.

To investigate the crystalline nature of the **Fe-HHB-w** film, scraped fragments were transferred onto copper grids through dispersion and drop-casting and further characterized by transmission electron microscopy (TEM). High-resolution TEM (HR-TEM) images (Figure 3a and Figure S8) reveal a well-preserved periodic structure throughout the entire area (∼10^4 nm^2), with no discernible defects observed within the highly ordered single-crystal hexagonal lattice. The corresponding fast Fourier transform (FFT) image exhibited a typical hexagonal diffraction pattern with a (100) plane distance of ∼6.6 Å, which matches well with the 2D Kagome lattice structure of the on-surface Fe-HHB nanodomains.[26] It is worth noting that the observed hexagonal structure is different from the 3D cubic structure of the in-solution synthesized Fe-THQ powders.[27,28] We temporarily attribute this discrepancy to the different synthesis environments (vapor phase vs solution phase), which could profoundly affect the topological structures and packing modes. For comparison, the crystallinity of the **Fe-HHB-o** samples synthesized in the absence of NH_3 was also examined. The sample exhibits smaller crystal domains (∼10^2 nm^2) with significant misorientation and large amorphous regions, indicating notably degraded film crystallinity (Figure 3b). As a result of the nearly 100-fold reduction in domain size, the electrical conductivity (σ) of **Fe-HHB-o** thin films decreases by approximately 3 orders of magnitude (∼2×10^{-3} S/cm) relative to **Fe-HHB-w** (∼3 S/cm), underscoring the critical role of crystallinity in determining charge transport properties (Figure S9).

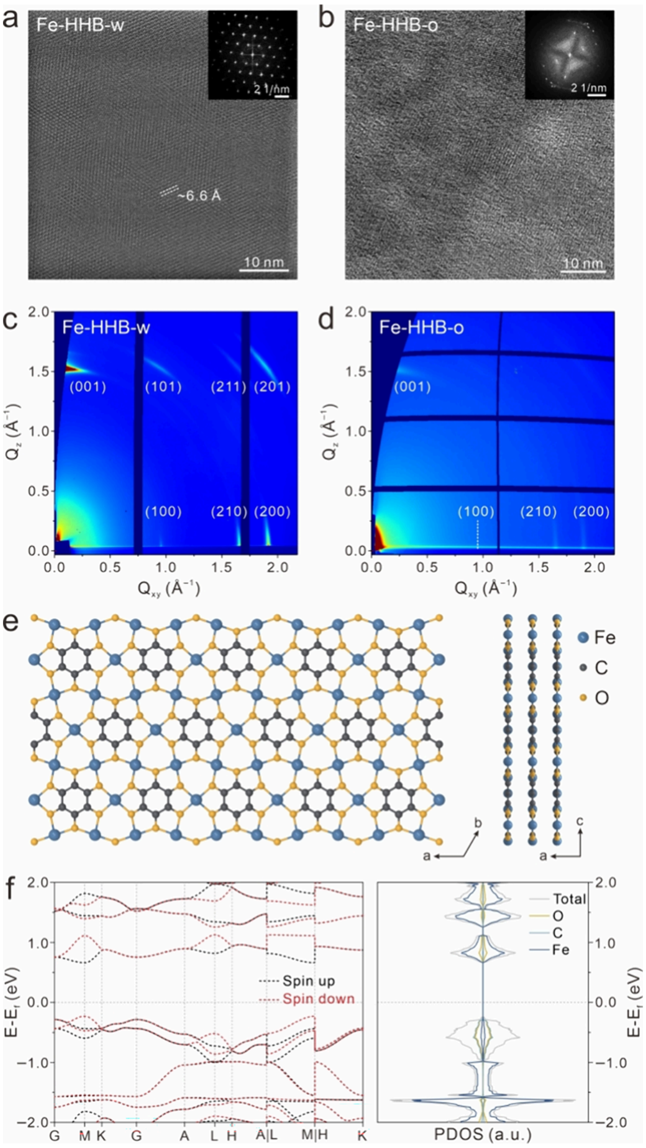

Figure 3. HR-TEM images acquired from (a) **Fe-HHB-w** and (b) **Fe-HHB-o** films. Insets show the corresponding FFT patterns. GIWAXS patterns of (c) **Fe-HHB-w** and (d) **Fe-HHB-o** films, with the corresponding peak assignments, were annotated. (e) AA-stacking model of the hexagonal Fe-HHB with a typical 2D Kagome lattice structure. (f) Calculated band structure of hexagonal Fe-HHB and the corresponding projected density of states (PDOS) for iron (blue), carbon (green), and oxygen (yellow). The Fermi energy was set to 0 eV.

Grazing-incidence wide-angle X-ray scattering (GIWAXS) measurements were also performed to characterize the crystallinity and analyze the lattice structure of the CVD thin films on a macroscopic scale. The 2D GIWAXS pattern of **Fe-HHB-w** shows more diffraction peaks with stronger signals compared to that of **Fe-HHB-o** with similar thickness (Figure 3c,d), indicating the formation of a film with inferior quality without the presence of NH_3. The significantly improved crystallinity enables a more detailed structural analysis based on the abundant crystal lattice information extracted from the GIWAXS pattern. As shown in Figure 3e, a 2D Kagome lattice structure with an AA-stacking model was established and then optimized by density functional theory (DFT) calculations (Figure S10), evidencing a typical hexagonal unit cell with lattice parameters of $a = b = 7.57$ Å. The three in-plane peaks observed at $Q_{xy} = 0.96$, 1.66, and 1.92 $Å^{-1}$ in Figure 3c can then be assigned to the (100), (210), and (200) planes of the hexagonal Fe-HHB lattice, respectively. The out-of-plane peak located at $Q_z = 1.53$ $Å^{-1}$ corresponds to the (001) plane along the $\pi-\pi$ stacking direction, which evidences a pronounced face-on layer orientation of the **Fe-HHB-w** film. Notably, synthesizing 2D CP and MOF films with face-on orientations is crucial for investigating their in-plane electronic transport properties. Compared to **Fe-HHB-w**, the broadening of the full width at half-maximum (fwhm) of the GIWAXS peaks extracted from **Fe-HHB-o** also suggests a reduced crystal domain size (Figure S11). The face-on oriented nature of the as-grown film enables us to observe the $\pi-\pi$ stacking peak in the powder X-ray diffraction (PXRD) spectrum,[29] which also reveals a broadened (001) peak in **Fe-HHB-o** samples (Figure S12).

The simulated GIWAXS result with a perfect face-on orientation matches the experimental pattern of **Fe-HHB-w** (Figure S13), thus validating the reliability of the proposed Fe-HHB lattice structure. Furthermore, the obtained selected area electron diffraction (SAED) pattern and the FFT pattern (inset of Figure 3a) of **Fe-HHB-w** along the [001] zone axis align well with the simulated electron diffraction pattern (Figure S14). The FFT pattern extracted from the HR-TEM image of the [100] zone axis was also consistent with the simulated pattern (Figure S15), thus further confirming the accuracy of the proposed Fe-HHB structure from the perspective of electron diffraction. To gain deeper insight into the electronic structure of Fe-HHB, spin-polarized DFT calculations based on its AA-stacking pattern were performed. As shown in Figure 3f, Fe-HHB possesses a direct bandgap of 0.89 eV with interlayer antiferromagnetic ordering. In addition, the ultraviolet-visible (UV−vis) spectrum presents an optical bandgap of ~1.3 eV (Figure S16), which also suggests its semiconducting feature.

The protons of HHB molecules would act as hindrances to obstruct the coordination bonding with Fe atoms owing to the electrostatic repulsion.[24] The deprotonation effect of NH_3 molecules effectively activates HHB molecules in the gas-phase reaction environment, thereby reducing the energy barrier for forming Fe−O coordination bonds and allowing for the smooth formation of ordered coordination networks. The X-ray photoelectron spectroscopy (XPS) analysis (Figure S17) of C 1s reveals a marked increase in the proportion of the C═O component in **Fe-HHB-o** compared to **Fe-HHB-w**, which is most likely due to a rise in uncoordinated O atoms during the formation of **Fe-HHB-o**. In addition, to exclude the possibility that the differences between **Fe-HHB-w** and **Fe-HHB-o** were induced by NH_3 doping, **Fe-HHB-o** films were treated in the optimal NH_3 atmosphere but showed no signs of increased conductivity (Figure S18).

To investigate the competing effect of NH_3, Fe-HHB thin films were synthesized under varying partial pressures of NH_3 gas. The statistical analyses of σ and (001) peak widths exhibit a similar bell-shaped trend as the NH_3 concentration rises (Figure S19), suggesting that amplifying the concentration beyond the optimal level could instead degrade the sample quality. The coordination between Fe with excess NH_3 could result in film quality deterioration, where the uncoordinated HHB molecules tend to self-assemble into crystals, as evidenced by the visible PXRD signals attributed to HHB (Figure S20). To further demonstrate the competing coordination effect of NH_3, the freshly synthesized **Fe-HHB-w** thin film was exposed to a high-concentration NH_3 atmosphere. The pronounced morphological changes and the presence of the N element on the film prove the reaction between NH_3 with the Fe-HHB coordination networks (Figure S21). The XPS N 1s spectrum revealed the presence of Fe-NH_3 coordination complexes and NH_4^+ species (Figure S22), thus confirming the role of NH_3 as an effective competing coordination species to regulate the formation and breakage of the Fe-HHB coordination bonds. Moreover, the roles of NH_3 in facilitating ligand deprotonation and serving as a competing coordination species are also applicable to the growth of Cu-HHB (Figures S23 and S24) and Cu-BHT (Figures S25 and S26) thin films with improved quality, as proven by the narrowing of PXRD peak width. The electrical conductivities of the Cu-HHB and Cu-BHT thin films were also increased from ~51 and ~595 to ~113 and ~905 S/cm, respectively, after adopting the NH_3-assisted strategy, validating the universality of the proposed strategy.

The high compatibility of the proposed CVD strategy with the device integration technologies ensures the easy fabrication of devices based on the as-grown films with large-area uniformity (Figure S27). To investigate the electrical properties of as-grown Fe-HHB films, four-probe devices were fabricated to measure the temperature-dependent σ. The results shown in Figure 4a revealed that the resistivity of both **Fe-HHB-w** and **Fe-HHB-o** negatively correlates with temperature (ranging from 295 to 573 K), consistent with their semiconducting nature. The data for **Fe-HHB-w** fits well with the Arrhenius equation (Figure 4b and Supporting Information), evidencing thermally activated transport behavior. Meanwhile, for **Fe-HHB-o** (Figure 4c), the linear correlation between ln σ and $T^{-1/4}$ suggests that charge transport within the film follows the variable range hopping (VRH) model, possibly originating from the presence of extensive amorphous regions.

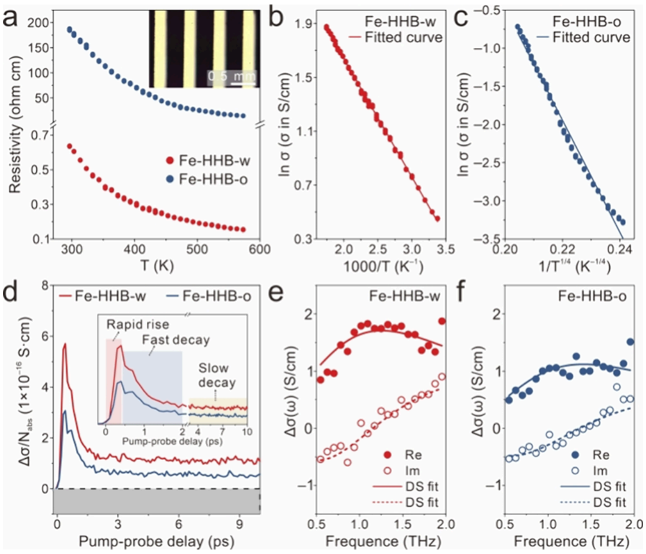

Figure 4. (a) Temperature-dependent electrical resistivity of the **Fe-HHB-w** and **Fe-HHB-o** thin films. The inset shows the OM image of the as-fabricated four-probe device. (b) Plot of ln σ versus T^{-1} for **Fe-HHB-w**. (c) Plot of ln σ versus $T^{-1/4}$ for **Fe-HHB-o**. (d) THz photoconductivity dynamics of **Fe-HHB-w** and **Fe-HHB-o** thin films normalized by N_{abs}. The inset shows the optimized plot of the same data, labeling the three distinct components of rapid rise, fast decay, and slow decay. The samples were photoexcited by an 800 nm laser pulse with a pump fluence of ~1.3 mJ/cm^2. The frequency-resolved complex photoconductivity of (e) **Fe-HHB-w** and (f) **Fe-HHB-o** was measured at ~0.5 ps after the maximum photoconductivity. The solid and hollow points are the real and imaginary components, respectively, and the solid and dashed lines represent the fitted DS curves.

Optical-pump THz-probe (OPTP) spectroscopy was utilized as an all-optical, noncontact approach to elucidate the microscopic charge transport properties of **Fe-HHB-w** (~99 nm thick) and **Fe-HHB-o** (~101 nm thick) thin films (Figure S28).[30] During the measurements, an ultrashort (~50 fs) 800 nm laser pulse optically injects charge carriers into the material by activating interband optical transitions. Subsequently, a time-delayed single-cycle THz pulse with a duration of ~1 ps interacts with the photogenerated charge carriers and interrogates their photoconductivity in a time- or frequency-resolved manner. As shown in Figure 4d, the photoconductivity ($\Delta\sigma$) of **Fe-HHB-w** and **Fe-HHB-o** was recorded as a function of pump−probe delay. Both samples exhibit a rapid rise in $\Delta\sigma$, reaching their maximum values on the subpicosecond time scale due to the quasi-instantaneous injection of mobile carriers. The photoconductivity then decays biexponentially, with a fast decay component vanishing within ~2 ps, followed by a slow decay component that persists without significant intensity attenuation for ~10 ps. The two decay components can be tentatively assigned to charge trapping and electron−hole recombination.[31] Compared with **Fe-HHB-o**, **Fe-HHB-w** exhibits higher $\Delta\sigma$ normalized by absorbed photon density (N_{abs}). Considering

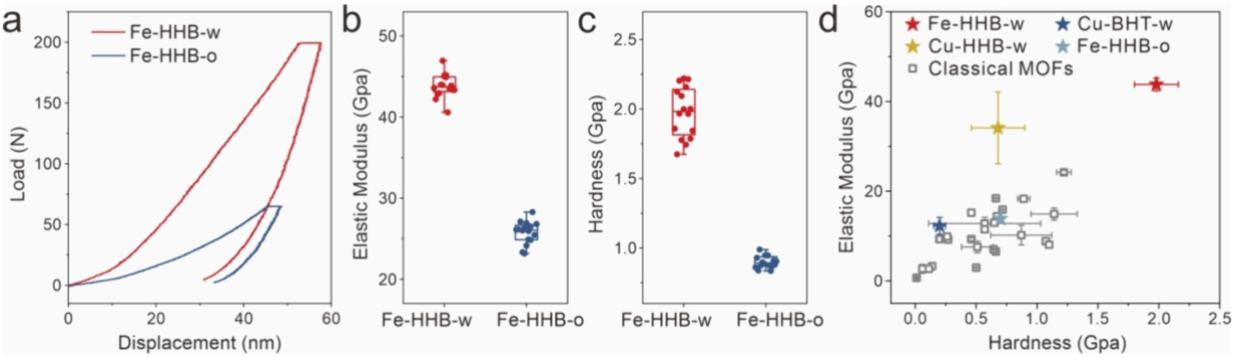

Figure 5. (a) Load−displacement curves of the **Fe-HHB-w** and **Fe-HHB-o** thin films. Statistical analysis of the (b) elastic modulus and (c) hardness of the two samples. (d) Property map of 2D c-CPs and MOFs showing the elastic modulus versus hardness. The CVD 2D c-CP thin films are labeled by stars with varied colors. The classical MOFs are labeled by gray rectangles. See Figure S29 for details.

that $\Delta\sigma/N_{\mathrm{abs}} = e\varphi\mu$ (e is the elementary charge and μ is the charge mobility), it can be inferred that **Fe-HHB-w** has a higher μ than **Fe-HHB-o**, assuming that they have similar φ.[32,33]

To gain more quantitative insights, the frequency-resolved complex photoconductivity of both samples was measured. Their spectral dispersions (Figure 4e,f) display a suppressed positive real part and a negative imaginary part at low frequencies, hallmarks of spatially confined charge transport as described by the Drude−Smith (DS) model (see the Supporting Information for a detailed discussion).[34] In the DS model, a backscattering parameter, c quantifies the degree of spatial confinement, with values ranging from −1 (preferential backscattering) to 0 (completely random momentum scattering). The best fits to the data yield scattering times (τ) of 116 ± 7 and 109 ± 8 fs and c values of −0.86 and −0.94 for **Fe-HHB-w** and **Fe-HHB-o**, respectively. The nonzero c values are consistent with the polycrystalline nature of the samples, where grain boundaries can contribute to backscattering that impedes long-range charge transport. Their charge mobilities in the dc limit (μ_{dc}) were estimated to be 31 ± 2 and 12 ± 1 $\mathrm{cm^2/(V{\cdot}s)}$, following $\mu_{\mathrm{dc}} = e\tau/m^*(1 + c)$, where e is the elementary charge and m^* ($m^* = 0.95\ m_0$) is the effective mass. The higher μ_{dc} of **Fe-HHB-w** can be attributed to the combined effect of a slightly increased τ and a reduction in backscattering events, likely due to suppressed charge scattering at grain boundaries. This aligns with the improved crystallinity observed in **Fe-HHB-w**, emphasizing that NH_3 plays a nontrivial role in improving the crystallinity and charge transport properties. The remarkable enhancement of electrical conductivities in **Cu-HHB-w** and **Cu-BHT-w** thin films (referring to the Cu-HHB and Cu-BHT samples grown by the NH_3-assisted strategy, respectively) is fundamentally attributed to the improved crystallinity, which generally promotes efficient charge transport.

Nanoindentation tests were then performed to evaluate the mechanical properties of Fe-HHB. As shown in the typical load−displacement curves (Figure 5a), the indentation depth of **Fe-HHB-w** was consistently lower than that of **Fe-HHB-o** under the same applied load, indicating a greater resistance to deformation. This is a plausible consequence of improved crystallinity, as the crystalline regions offer greater structural integrity and resistance to dislocation movement. Ensured by the high dissociation energy of Fe−O bonds, an elastic modulus of ∼43.8 GPa (Figure 5b) and an average hardness of ∼2.0 GPa (Figure 5c) were extracted for **Fe-HHB-w** thin films, significantly surpassing those of **Fe-HHB-o** (average elastic modulus of ∼25.7 GPa and hardness of ∼0.9 GPa), **Cu-HHB-w**, **Cu-BHT-w**, and the reported traditional MOFs (Figure 5d and Figure S29).[35] The superior mechanical performance makes **Fe-HHB-w** thin films suitable for electronic applications requiring wear-resistant active materials such as high-durability wearable devices.

■ CONCLUSIONS

In conclusion, we have demonstrated that leveraging the deprotonation effect and coordination competing effect of NH_3 can significantly enhance the crystallinity of as-grown 2D c-CP samples, enabling the formation of Fe-HHB, Cu-HHB, and Cu-BHT thin films with noticeably elevated electrical and mechanical properties. In addition to universally producing high-quality thin films with large-area uniformity, our method also shows high compatibility with typical device integration technologies, laying a foundation for exploring the fascinating properties of 2D c-CPs and advancing their practical applications. We believe that our proposed synthetic strategy affords feasible access to operational 2D conductive CP and MOF thin films and provides the opportunity to develop CP/MOF electronics.

■ ASSOCIATED CONTENT

Supporting Information

The Supporting Information is available free of charge at https://pubs.acs.org/doi/10.1021/jacs.5c04515.

> The Supporting Information is available free of charge on the ACS Publications Web site.
>
> General information on methods and characterizations, additional discussion of Arrhenius fitting and OPTP measurements, and supplemental figures (PDF)

■ AUTHOR INFORMATION

Corresponding Authors

Xinliang Feng − *Max Planck Institute for Microstructure Physics, Halle (Saale) 06120, Germany; Center for Advancing Electronics Dresden and Faculty of Chemistry and Food Chemistry, TUD Dresden University of Technology, Dresden 01067, Germany;* orcid.org/0000-0003-3885-2703; Email: xinliang.feng@tu-dresden.de

Renhao Dong − *Department of Chemistry, The University of Hong Kong, Hong Kong 999077, China; Materials*

Innovation Institute for Life Sciences and Energy (MILES), HKU-SIRI, Shenzhen 518048, China; orcid.org/0000-0002-4125-9284; Email: rhdong@hku.hk

Authors

Jinxin Liu − *Max Planck Institute for Microstructure Physics, Halle (Saale) 06120, Germany*

Shuai Fu − *Center for Advancing Electronics Dresden and Faculty of Chemistry and Food Chemistry, TUD Dresden University of Technology, Dresden 01067, Germany; Max Planck Institute for Polymer Research, Mainz 55128, Germany*

Yubin Fu − *Max Planck Institute for Microstructure Physics, Halle (Saale) 06120, Germany; Center for Advancing Electronics Dresden and Faculty of Chemistry and Food Chemistry, TUD Dresden University of Technology, Dresden 01067, Germany;* orcid.org/0000-0002-2613-394X

Yunxu Chen − *Max Planck Institute for Microstructure Physics, Halle (Saale) 06120, Germany*

Kian Tadayon − *Fraunhofer Institute for Ceramic Technologies and Systems (IKTS), Dresden 01109, Germany*

Mike Hambsch − *Center for Advancing Electronics Dresden (CFAED) and Faculty of Electrical and Computer Engineering, TUD Dresden University of Technology, Dresden 01062, Germany;* orcid.org/0000-0002-8487-0972

Darius Pohl − *Dresden Center for Nanoanalysis (DCN), Center for Advancing Electronics Dresden (CFAED), TUD Dresden University of Technology, Dresden 01069, Germany*

Ye Yang − *Center for Advancing Electronics Dresden and Faculty of Chemistry and Food Chemistry, TUD Dresden University of Technology, Dresden 01067, Germany*

Alina Müller − *Center for Advancing Electronics Dresden and Faculty of Chemistry and Food Chemistry, TUD Dresden University of Technology, Dresden 01067, Germany*

Fengxiang Zhao − *Department of Chemistry, The University of Hong Kong, Hong Kong 999077, China; Materials Innovation Institute for Life Sciences and Energy (MILES), HKU-SIRI, Shenzhen 518048, China*

Stefan C. B. Mannsfeld − *Center for Advancing Electronics Dresden (CFAED) and Faculty of Electrical and Computer Engineering, TUD Dresden University of Technology, Dresden 01062, Germany;* orcid.org/0000-0003-0268-519X

Lei Gao − *Max Planck Institute for Polymer Research, Mainz 55128, Germany*

Mischa Bonn − *Max Planck Institute for Polymer Research, Mainz 55128, Germany;* orcid.org/0000-0001-6851-8453

Complete contact information is available at:
https://pubs.acs.org/10.1021/jacs.5c04515

Author Contributions

‡J.L., S.F., and Y.F. contributed equally to this work.

Notes

The authors declare no competing financial interest.

■ ACKNOWLEDGMENTS

This work was financially supported by the National Key R&D Program of China (no. 2024YFB4006800), ERC starting grant (FC2DMOF, no. 852909), National Natural Science Foundation of China (nos. 22272092 and 22472085), SFB-1415 (no. 417590517), GRK2861 (no. 491865171), and the German Science Council, Center for Advancing Electronics Dresden (CFAED). This project has received funding from the European Research Council (ERC) under the European Union's Horizon 2020 research and innovation programme (ERC grant agreement no. 714067, ENERGYMAPS). We acknowledge the European Synchrotron Radiation Facility (ESRF) for the provision of synchrotron radiation facilities, and we would like to thank Dr. Oleg Konovalov for assistance and support in using beamline ID10. We acknowledge SOLEIL for the provision of synchrotron radiation facilities, and we would like to thank Dr. Arnaud Hemmerle for assistance in using beamline SIRIUS. We acknowledge the Dresden Center for Nanoanalysis (DCN) at TUD. R.D. thanks the Taishan Scholars Program of Shandong Province (tsqn201909047), Natural Science Foundation of Shandong Province (ZR2023JQ005), and Materials Innovation Institute for Life Sciences and Energy (MILES), HKU-SIRI. M.H. and S.C.B.M. would like to thank Dr. Shaoling Bai and Jonathan Perez for their help with the GIWAXS measurements. We gratefully acknowledge the GWK support for funding this project by providing computing time through the Centre for Information Services and HPC (ZIH) at TU Dresden.

■ REFERENCES

(1) Sun, L.; Miyakai, T.; Seki, S.; Dincă, M. Mn_2(2,5-Disulfhydrylbenzene-1,4-Dicarboxylate): A Microporous Metal−Organic Framework with Infinite $(-Mn-S-)_\infty$ Chains and High Intrinsic Charge Mobility. *J. Am. Chem. Soc.* **2013**, *135* (22), 8185−8188.

(2) Talin, A. A.; Centrone, A.; Ford, A. C.; Foster, M. E.; Stavila, V.; Haney, P.; Kinney, R. A.; Szalai, V.; El Gabaly, F.; Yoon, H. P.; Léonard, F.; Allendorf, M. D. Tunable Electrical Conductivity in Metal-Organic Framework Thin-Film Devices. *Science* **2014**, *343* (6166), 66−69.

(3) Yan, X.; Su, X.; Chen, J.; Jin, C.; Chen, L. Two-Dimensional Metal-Organic Frameworks Towards Spintronics. *Angew. Chem., Int. Ed.* **2023**, *62* (41), No. e202305408.

(4) Xie, L. S.; Skorupskii, G.; Dincă, M. Electrically Conductive Metal-Organic Frameworks. *Chem. Rev.* **2020**, *120* (16), 8536−8580.

(5) Wang, M.; Dong, R.; Feng, X. Two-Dimensional Conjugated Metal-Organic Frameworks (2D c-MOFs): Chemistry and Function for MOFtronics. *Chem. Soc. Rev.* **2021**, *50* (4), 2764−2793.

(6) Huang, X.; Sheng, P.; Tu, Z.; Zhang, F.; Wang, J.; Geng, H.; Zou, Y.; Di, C. A.; Yi, Y.; Sun, Y.; Xu, W.; Zhu, D. A Two-Dimensional π-d Conjugated Coordination Polymer with Extremely High Electrical Conductivity and Ambipolar Transport Behaviour. *Nat. Commun.* **2015**, *6* (1), 7408.

(7) Dong, R.; Han, P.; Arora, H.; Ballabio, M.; Karakus, M.; Zhang, Z.; Shekhar, C.; Adler, P.; Petkov, P. S.; Erbe, A.; Mannsfeld, S. C. B.; Felser, C.; Heine, T.; Bonn, M.; Feng, X.; Cánovas, E. High-Mobility Band-like Charge Transport in a Semiconducting Two-Dimensional Metal−Organic Framework. *Nat. Mater.* **2018**, *17* (11), 1027−1032.

(8) Huang, X.; Zhang, S.; Liu, L.; Yu, L.; Chen, G.; Xu, W.; Zhu, D. Superconductivity in a Copper(II)-Based Coordination Polymer with Perfect Kagome Structure. *Angew. Chem., Int. Ed.* **2018**, *57* (1), 146−150.

(9) Arora, H.; Dong, R.; Venanzi, T.; Zscharschuch, J.; Schneider, H.; Helm, M.; Feng, X.; Cánovas, E.; Erbe, A. Demonstration of a Broadband Photodetector Based on a Two-Dimensional Metal−Organic Framework. *Adv. Mater.* **2020**, *32* (9), 1907063.

(10) Dong, R.; Zhang, Z.; Tranca, D. C.; Zhou, S.; Wang, M.; Adler, P.; Liao, Z.; Liu, F.; Sun, Y.; Shi, W.; Zhang, Z.; Zschech, E.; Mannsfeld, S. C. B.; Felser, C.; Feng, X. A Coronene-Based Semiconducting Two-Dimensional Metal-Organic Framework with Ferromagnetic Behavior. *Nat. Commun.* **2018**, *9* (1), 2637.

(11) Liu, J.; Chen, Y.; Feng, X.; Dong, R. Conductive 2D Conjugated Metal−Organic Framework Thin Films: Synthesis and Functions for (Opto-)Electronics. *Small Struct.* **2022**, *3* (5), 2100210.

(12) Wang, L.; Sahabudeen, H.; Zhang, T.; Dong, R. Liquid-Interface-Assisted Synthesis of Covalent-Organic and Metal-Organic Two-Dimensional Crystalline Polymers. *npj 2D Mater. Appl.* **2018**, *2* (1), 26.

(13) Stassen, I.; Styles, M.; Grenci, G.; Gorp, H. V.; Vanderlinden, W.; Feyter, S. D.; Falcaro, P.; Vos, D. D.; Vereecken, P.; Ameloot, R. Chemical Vapour Deposition of Zeolitic Imidazolate Framework Thin Films. *Nat. Mater.* **2016**, *15* (3), 304−310.

(14) Su, P.; Tu, M.; Ameloot, R.; Li, W. Vapor-Phase Processing of Metal−Organic Frameworks. *Acc. Chem. Res.* **2022**, *55* (2), 186−196.

(15) Stassen, I.; Burtch, N.; Talin, A.; Falcaro, P.; Allendorf, M.; Ameloot, R. An Updated Roadmap for the Integration of Metal−Organic Frameworks with Electronic Devices and Chemical Sensors. *Chem. Soc. Rev.* **2017**, *46* (11), 3185−3241.

(16) Sun, L.; Yuan, G.; Gao, L.; Yang, J.; Chhowalla, M.; Gharahcheshmeh, M. H.; Gleason, K. K.; Choi, Y. S.; Hong, B. H.; Liu, Z. Chemical Vapour Deposition. *Nat. Rev. Methods Primers* **2021**, *1* (1), 5.

(17) Zeng, M.; Liu, J.; Zhou, L.; Mendes, R. G.; Dong, Y.; Zhang, M.-Y.; Cui, Z.-H.; Cai, Z.; Zhang, Z.; Zhu, D.; Yang, T.; Li, X.; Wang, J.; Zhao, L.; Chen, G.; Jiang, H.; Rümmeli, M. H.; Zhou, H.; Fu, L. Bandgap Tuning of Two-Dimensional Materials by Sphere Diameter Engineering. *Nat. Mater.* **2020**, *19* (5), 528−533.

(18) Zhao, T.; Guo, J.; Li, T.; Wang, Z.; Peng, M.; Zhong, F.; Chen, Y.; Yu, Y.; Xu, T.; Xie, R.; Gao, P.; Wang, X.; Hu, W. Substrate Engineering for Wafer-Scale Two-Dimensional Material Growth: Strategies, Mechanisms, and Perspectives. *Chem. Soc. Rev.* **2023**, *52* (5), 1650−1671.

(19) Rubio-Giménez, V.; Arnauts, G.; Wang, M.; Oliveros Mata, E. S.; Huang, X.; Lan, T.; Tietze, M. L.; Kravchenko, D. E.; Smets, J.; Wauteraerts, N.; Khadiev, A.; Novikov, D. V.; Makarov, D.; Dong, R.; Ameloot, R. Chemical Vapor Deposition and High-Resolution Patterning of a Highly Conductive Two-Dimensional Coordination Polymer Film. *J. Am. Chem. Soc.* **2023**, *145* (1), 152−159.

(20) Liu, J.; Chen, Y.; Huang, X.; Ren, Y.; Hambsch, M.; Bodesheim, D.; Pohl, D.; Li, X.; Deconinck, M.; Zhang, B.; Löffler, M.; Liao, Z.; Zhao, F.; Dianat, A.; Cuniberti, G.; Vaynzof, Y.; Gao, J.; Hao, J.; Mannsfeld, S. C. B.; Feng, X.; Dong, R. On-Liquid-Gallium Surface Synthesis of Ultrasmooth Thin Films of Conductive Metal−Organic Frameworks. *Nat. Synth.* **2024**, *3* (6), 715−726.

(21) Ogle, J.; Lahiri, N.; Jaye, C.; Tassone, C. J.; Fischer, D. A.; Louie, J.; Whittaker-Brooks, L. Semiconducting to Metallic Electronic Landscapes in Defects-Controlled 2D π-d Conjugated Coordination Polymer Thin Films. *Adv. Funct. Mater.* **2021**, *31* (4), 2006920.

(22) Choe, M.; Koo, J. Y.; Park, I.; Ohtsu, H.; Shim, J. H.; Choi, H. C.; Park, S. S. Chemical Vapor Deposition of Edge-on Oriented 2D Conductive Metal−Organic Framework Thin Films. *J. Am. Chem. Soc.* **2022**, *144* (37), 16726−16731.

(23) Choe, M.; Park, S. S.; Choi, H. C. Elucidation of the Transformation of Coordination Polymer Intermediates into 2D Metal−Organic Framework Films during Chemical Vapor Deposition. *Inorg. Chem.* **2024**, *63* (48), 22662−22666.

(24) Keene, F. R.; Szalda, D. J.; Wilson, T. A. Mode of Coordination of Tris(2-Pyridyl)Methanol to Ruthenium(II): Synthetic, Spectral, and Structural Studies of the Bis(Ligand) Species. *Inorg. Chem.* **1987**, *26* (14), 2211−2216.

(25) Amores, M.; Wada, K.; Sakaushi, K.; Nishihara, H. Reversible Energy Storage in Layered Copper-Based Coordination Polymers: Unveiling the Influence of the Ligand's Functional Group on Their Electrochemical Properties. *J. Phys. Chem. C* **2020**, *124* (17), 9215−9224.

(26) Hua, M.; Xia, B.; Wang, M.; Li, E.; Liu, J.; Wu, T.; Wang, Y.; Li, R.; Ding, H.; Hu, J.; Wang, Y.; Zhu, J.; Xu, H.; Zhao, W.; Lin, N. Highly Degenerate Ground States in a Frustrated Antiferromagnetic Kagome Lattice in a Two-Dimensional Metal−Organic Framework. *J. Phys. Chem. Lett.* **2021**, *12* (15), 3733−3739.

(27) Chen, G.; Gee, L. B.; Xu, W.; Zhu, Y.; Lezama-Pacheco, J. S.; Huang, Z.; Li, Z.; Babicz, J. T., Jr.; Choudhury, S.; Chang, T.-H.; Reed, E.; Solomon, E. I.; Bao, Z. Valence-Dependent Electrical Conductivity in a 3D Tetrahydroxyquinone-Based Metal−Organic Framework. *J. Am. Chem. Soc.* **2020**, *142* (51), 21243−21248.

(28) Wu, X.; Qiu, Y.; Chen, Z.; Guan, B.; Hao, X.; Rykov, A. I.; Sun, Y.; Liu, L.; Zou, Y.; Sun, J.; Xu, W.; Zhu, D. Paramagnetic Conducting Metal−Organic Frameworks with Three-Dimensional Structure. *Angew. Chem., Int. Ed.* **2020**, *59* (47), 20873−20878.

(29) Holder, C. F.; Schaak, R. E. Tutorial on Powder X-Ray Diffraction for Characterizing Nanoscale Materials. *ACS Nano* **2019**, *13* (7), 7359−7365.

(30) Ulbricht, R.; Hendry, E.; Shan, J.; Heinz, T. F.; Bonn, M. Carrier Dynamics in Semiconductors Studied with Time-Resolved Terahertz Spectroscopy. *Rev. Mod. Phys.* **2011**, *83* (2), 543−586.

(31) Huang, X.; Li, Y.; Fu, S.; Ma, C.; Lu, Y.; Wang, M.; Zhang, P.; Li, Z.; He, F.; Huang, C.; Liao, Z.; Zou, Y.; Zhou, S.; Helm, M.; Petkov, P. S.; Wang, H. I.; Bonn, M.; Li, J.; Xu, W.; Dong, R.; Feng, X. Control of the Hydroquinone/Benzoquinone Redox State in High-Mobility Semiconducting Conjugated Coordination Polymers. *Angew. Chem., Int. Ed.* **2024**, *63* (20), No. e202320091.

(32) Dubey, R. K.; Marongiu, M.; Fu, S.; Wen, G.; Bonn, M.; Wang, H. I.; Melle-Franco, M.; Mateo-Alonso, A. Accelerated Iterative Synthesis of Ultralong Graphene Nanoribbons with Full Atomic Precision. *Chem.* **2023**, *9* (10), 2983−2996.

(33) Lu, Y.; Hu, Z.; Petkov, P.; Fu, S.; Qi, H.; Huang, C.; Liu, Y.; Huang, X.; Wang, M.; Zhang, P.; Kaiser, U.; Bonn, M.; Wang, H. I.; Samorì, P.; Coronado, E.; Dong, R.; Feng, X. Tunable Charge Transport and Spin Dynamics in Two-Dimensional Conjugated Metal−Organic Frameworks. *J. Am. Chem. Soc.* **2024**, *146* (4), 2574−2582.

(34) Smith, N. V. Drude Theory and the Optical Properties of Liquid Mercury. *Phys. Lett. A* **1968**, *26* (3), 126−127.

(35) Burtch, N. C.; Heinen, J.; Bennett, T. D.; Dubbeldam, D.; Allendorf, M. D. Mechanical Properties in Metal−Organic Frameworks: Emerging Opportunities and Challenges for Device Functionality and Technological Applications. *Adv. Mater.* **2018**, *30* (37), 1704124.